Reduction in Human Activity can Enhance the Urban Heat Island: Insights from the COVID-19 Lockdown – Supplementary Material

TC Chakraborty

School of the Environment, Yale University, New Haven, CT 06511, USA

Chandan Sarangi*

Department of Civil Engineering, Indian Institute of Technology, Madras, Chennai 600036. Tamil Nadu, INDIA

Xuhui Lee*

School of the Environment, Yale University, New Haven, CT 06511, USA

*Corresponding authors: Chandan Sarangi (chandansarangi@civil.iitm.ac.in) & Xuhui Lee (xuhui.lee@yale.edu)

Supplementary Materials

The Intrinsic Biophysical Mechanism

Since satellite-derived observations are only valid for clear-sky conditions, we employ the Intrinsic Biophysical Mechanism (IBPM) [1] to diagnose the reasons for the change in the rural surface climate in the region for all-sky conditions. The IBPM theory solves the surface energy budget to isolate the different drivers of ΔLST. The surface energy budget is given by:

$$K_{\downarrow} + L_{\downarrow} - K_{\uparrow} - L_{\uparrow} = H + \lambda E + G \quad (1)$$

Here, $K_{\downarrow}$ is the incoming shortwave radiative flux, $L_{\downarrow}$ is the incoming longwave radiative flux, $K_{\uparrow}$ is the surface reflected shortwave radiation flux, $L_{\uparrow}$ is the surface emitted longwave radiative flux, H is the sensible heat flux, λE is the latent heat flux, and G is the ground flux. The left-hand side of Eq 1 represent the surface net radiation (R_n).

The perturbation in LST can be due to either a change in the energy input to the system ($K\downarrow$ and $L\downarrow$) or a redistribution of the energy through convection (H) and/or evaporation (λE). The total LST change (ΔLST) due to a forcing agent is the sum of the changes in the blending height temperature (ΔBHT) and the local temperature response (ΔT):

$$\Delta\text{LST} = \Delta T + \Delta\text{BHT} \quad (2)$$

Here the blending height is the height at which the vertical profiles of atmospheric variables are horizontally blended and no longer influenced by surface heterogeneity. For this study, the blending height is derived from the lowest model level in MERRA-2 (985 hPa) [2]. The conceptual assumption follows that, ignoring larger-scale feedback, changes in ΔBHT are due to atmospheric processes, while changes in ΔT are controlled by the Earth's land surface processes.

The local temperature response due to these surface processes is given by:

$$\Delta T = \frac{\lambda_0}{1+f}\Delta K_{\downarrow}(1-a) + \frac{\lambda_0}{1+f}\Delta L_{\downarrow} + \frac{-\lambda_0}{(1+f)^2}(R_{\mathrm{n}}^{*} - G)\Delta f_1 + \frac{-\lambda_0}{(1+f)^2}(R_{\mathrm{n}}^{*} - G)\Delta f_2 + \frac{\lambda_0}{1+f}\Delta G \quad (3)$$

The terms on the right-hand side of Eq. 3 represent these pathways, and from left to right, are the temperature response due to the shortwave radiative forcing, the longwave radiative forcing, energy redistribution through evaporation, energy redistribution through convection, and change in ground heat flux. Here, $\Delta K_{\downarrow}$ is the change in incoming shortwave radiation, ΔL is the change in absorbed longwave radiation, and ΔG is the change in ground heat flux. Since R_n is dependent on LST (through the $L\uparrow$ term), we define an apparent net radiation (R_{n}^{*}) that is not a function of the land surface temperature by replacing LST with BHT.

$$R_{\mathrm{n}}^{*} = K_{\downarrow}(1-a) + L_{\downarrow} - \varepsilon\sigma BHT^{4} \quad (4)$$

where ε is the surface emissivity and σ is the Stefan Boltzmann constant (5.67×10^{-8} W m^{-2} K^{-4}). λ_0 is the temperature sensitivity due to longwave feedback, derived by differentiating the Stefan-Boltzmann law, and given by:

$$\lambda_0 = \frac{1}{4\sigma LST^{3}} \quad (5)$$

and f is a factor denoting energy redistribution through non-radiative pathways, calculated using:

$$f = \frac{\lambda_0}{LST - BHT}\,(R_{\mathrm{n}}^{*} - G) - 1 \quad (6)$$

The change in f due to evaporative (Δf_1) and convection (Δf_2) can be calculated from:

$$\Delta f_1 = -f\frac{\Delta\beta}{\beta(1+\beta)} \quad (7)$$

$$\Delta f_2 = -f\frac{\Delta r_{\mathrm{a}}}{r_{\mathrm{a}}} \quad (8)$$

where β is the Bowen ratio, the ratio of H and λE, and r_a is the aerodynamic resistance, formulated by inverting the equation for H as:

$$r_{\mathrm{a}} = \frac{\rho C_p (LST - BHT)}{H} \quad (9)$$

Here, ρ is the air density, and C_p is the specific heat capacity of air at constant pressure. All the perturbation terms were calculated from the MERRA-2 reanalysis as the difference between the 5-year baseline and the lockdown period. f and λ_0 were calculated for the baseline period, while β, r_a, and λ_0 are the averages of the two periods. Since f cannot physically have a negative value, the grids with $f < 0$ are excluded from the analysis.

References

1. Lee X *et al* 2011 Observed increase in local cooling effect of deforestation at higher latitudes *Nature* **479** 384–7 10.1038/nature10588
2. Chakraborty T and Lee X 2019 Land cover regulates the spatial variability of temperature response to the direct radiative effect of aerosols *Geophys. Res. Lett.* **46** 8995–9003 10.1029/2019GL083812

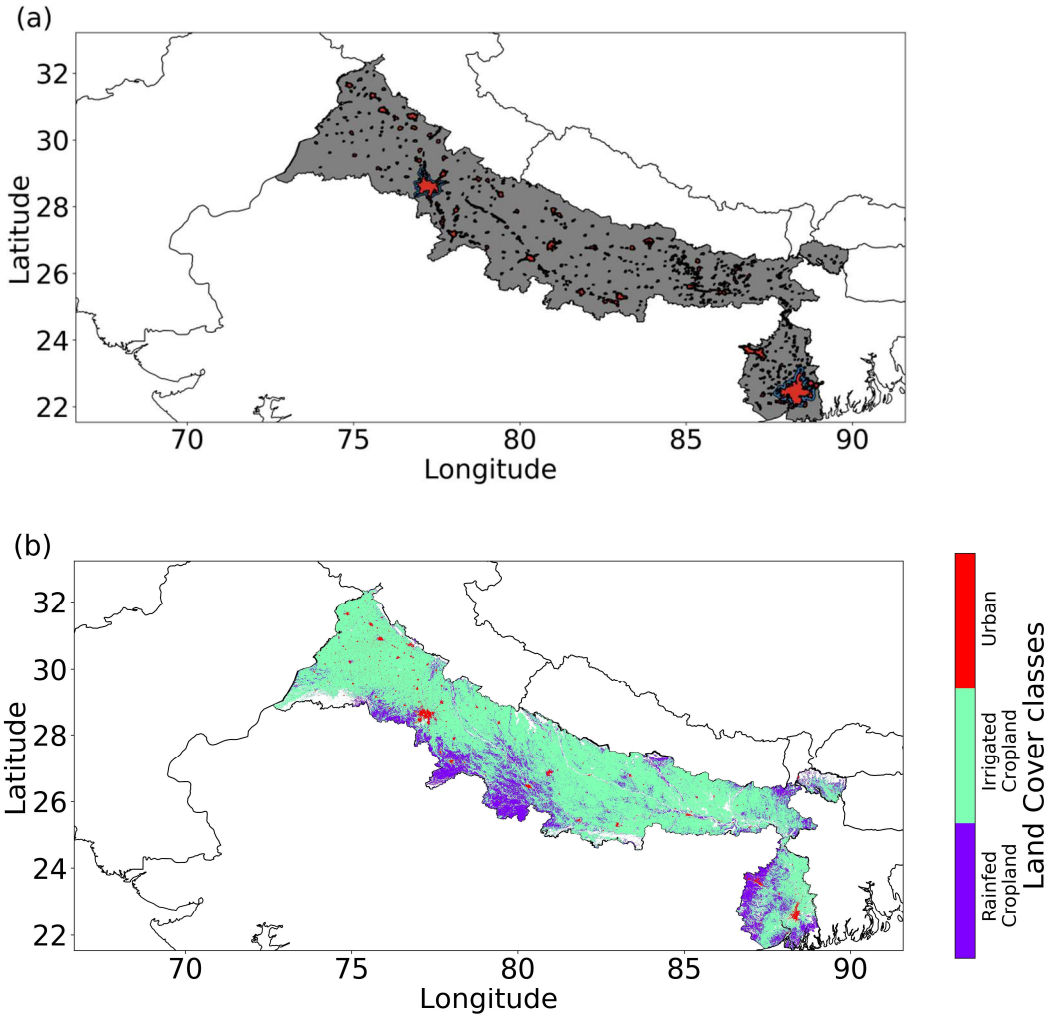

Figure S1: Map of study area. The black polygon in sub-figure (a) show the Indo-Gangetic Basin (IGB). The generated urban clusters are in red, while their corresponding normalized rural buffers are shown in blue. Sub-figure (b) shows the distribution of three relevant land cover categories for the IGB from the European Space Agency Climate Change Initiative land cover dataset for 2018.

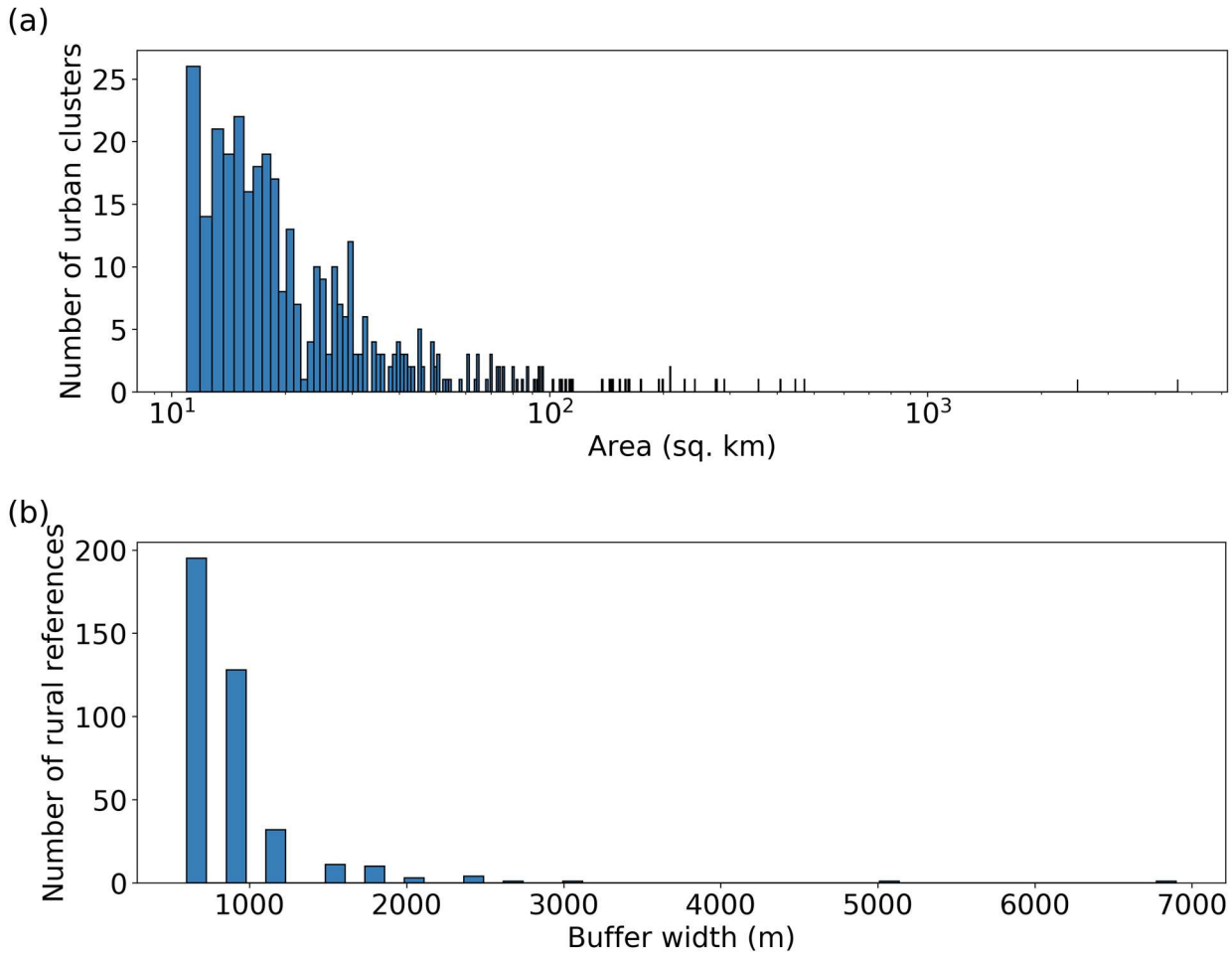

Figure S2: Distribution of urban and rural units of calculations used in the study. Sub-figure (a) shows the density plot of the urban clusters with areas greater than 1 km^2 used in the study after cloud screening of the data. Sub-figure (b) shows the distribution of the buffer widths used to calculate the rural references following the integration procedure used to minimize area difference between urban areas and their references.

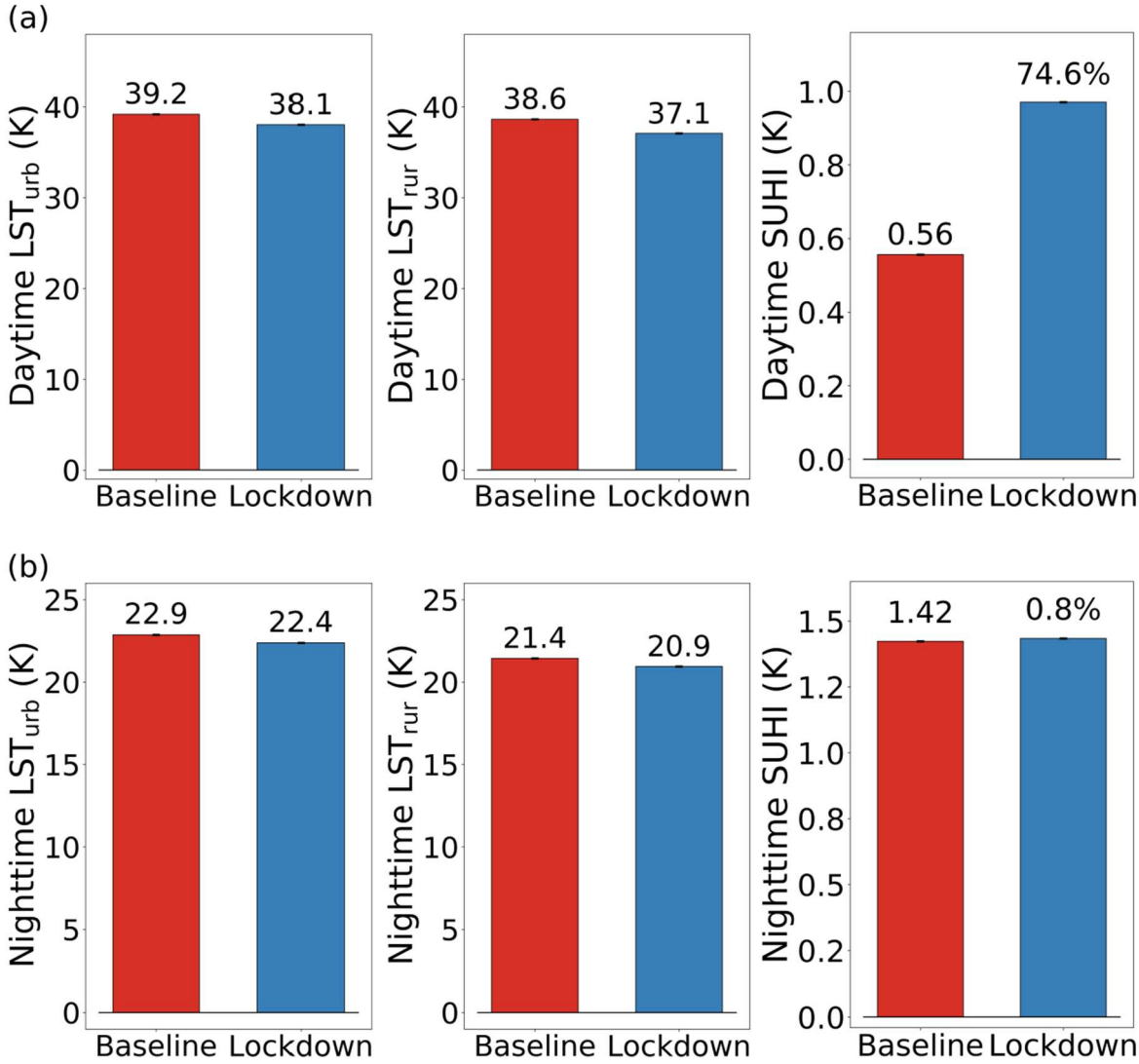

Figure S3: Perturbations to land surface temperature (LST) and surface urban heat island (SUHI) intensity. Sub-figures (a) and (b) show the mean (weighted by urban cluster area) land surface temperature (LST) and surface urban heat island (SUHI for urban clusters and their rural references for the baseline period, as well as their perturbed values during the lockdown period, for daytime and nighttime, respectively. The values above the bars show the mean values (percentage change during lockdown period for SUHI) and the error bars represent the 95% confidence interval of the area-weighted mean.

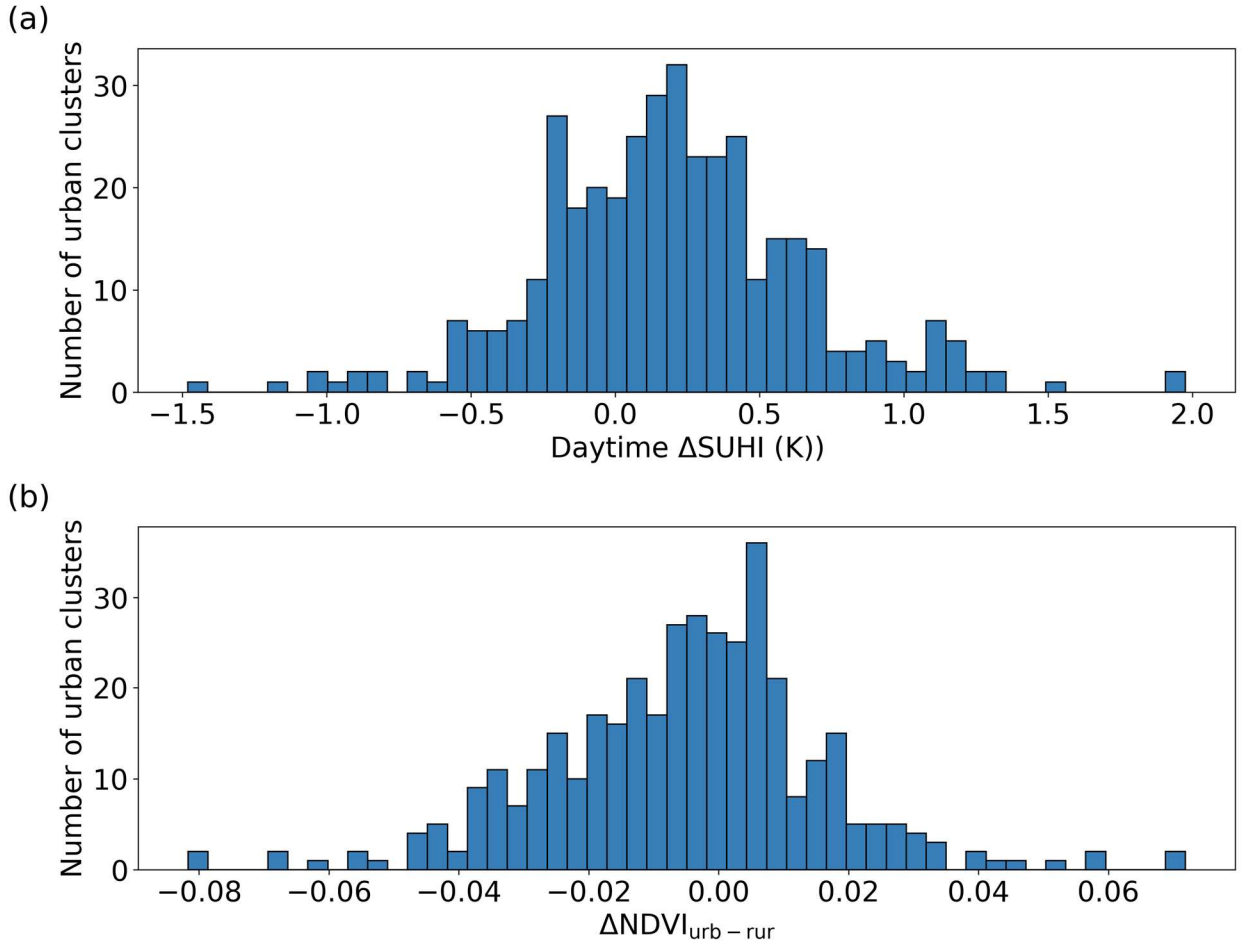

Figure S4: Distribution of (a) daytime ΔSUHI and (b) $\Delta NDVI_{urb\text{-}rur}$ among the urban clusters used in the study.

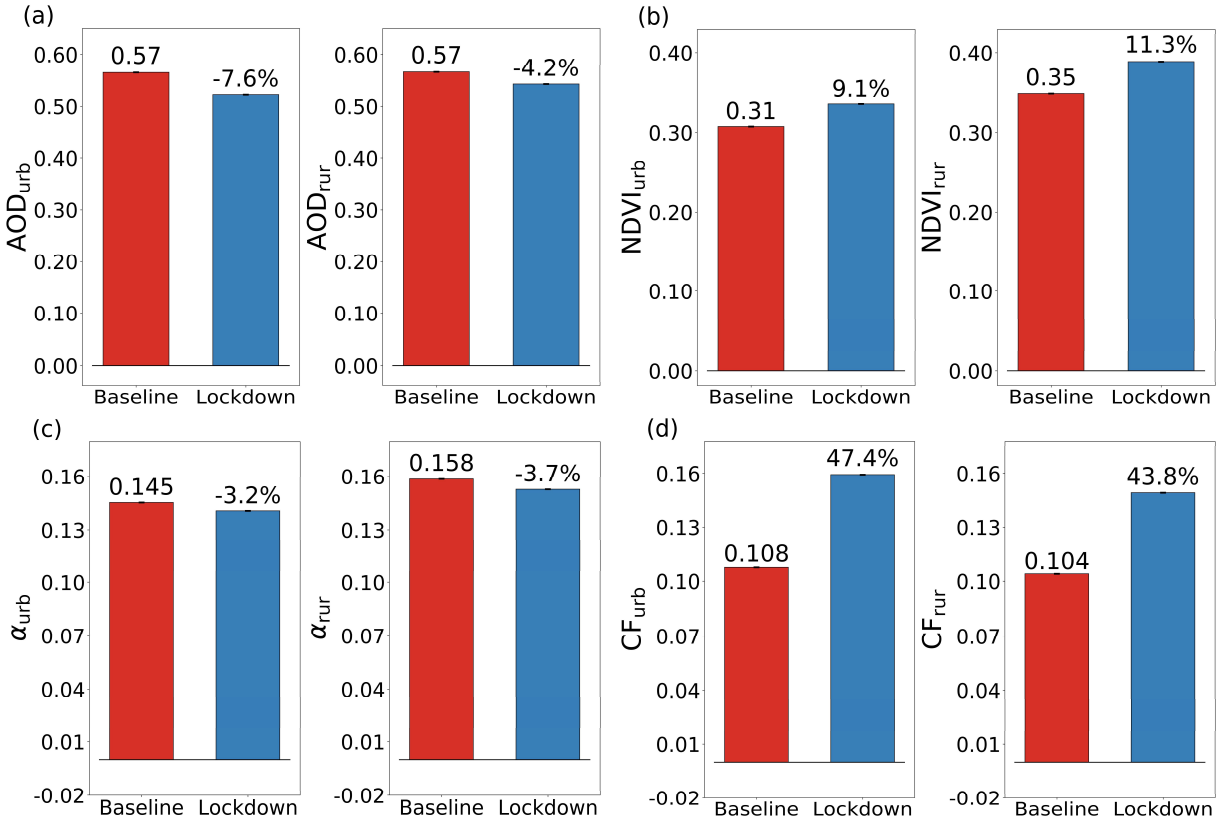

Figure S5: Changes in major surface and atmospheric factors. Sub-figures (a), (b), (c), and (d) show the mean (weighted by urban cluster area) Aerosol Optical Depth (AOD), normalized difference vegetation index (NDVI), surface albedo (α), and cloud fraction (CF) for urban clusters and their rural references for the baseline period, as well as their perturbed values during the lockdown. The values above the bars show the mean values for the baseline period (2015-2019 baseline for everything other than CF; 2019 baseline for CF) and the percentage change from that value. The error bars represent the 95% confidence interval of the area-weighted mean. The values shown here are also summarized in Table S1.

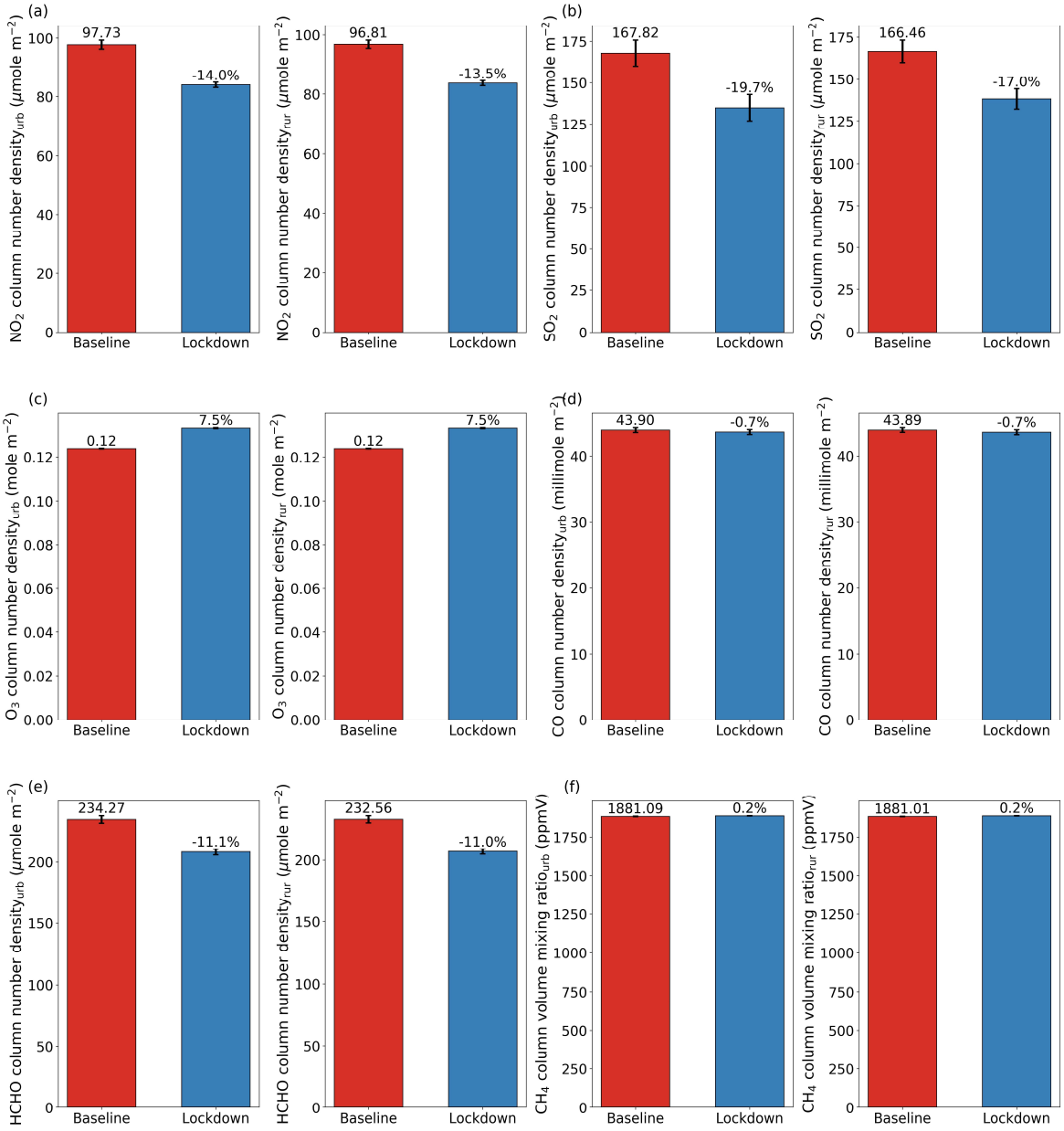

Figure S6: Sub-figures (a), (b), (c), (d), (e), and (f) show the mean (weighted by urban cluster area) Nitrogen Dioxide (NO_2), Sulphur Dioxide (SO_2), Ozone (O_3), Carbon Monoxide (CO), Formaldehyde (HCHO), and Methane (CH_4) concentrations for urban clusters and their rural references for the 2019 baseline, as well as their perturbed values during the lockdown. The values above the bars show the mean values for the baseline period and the percentage change from that value. The error bars represent the 95% confidence interval of the mean.

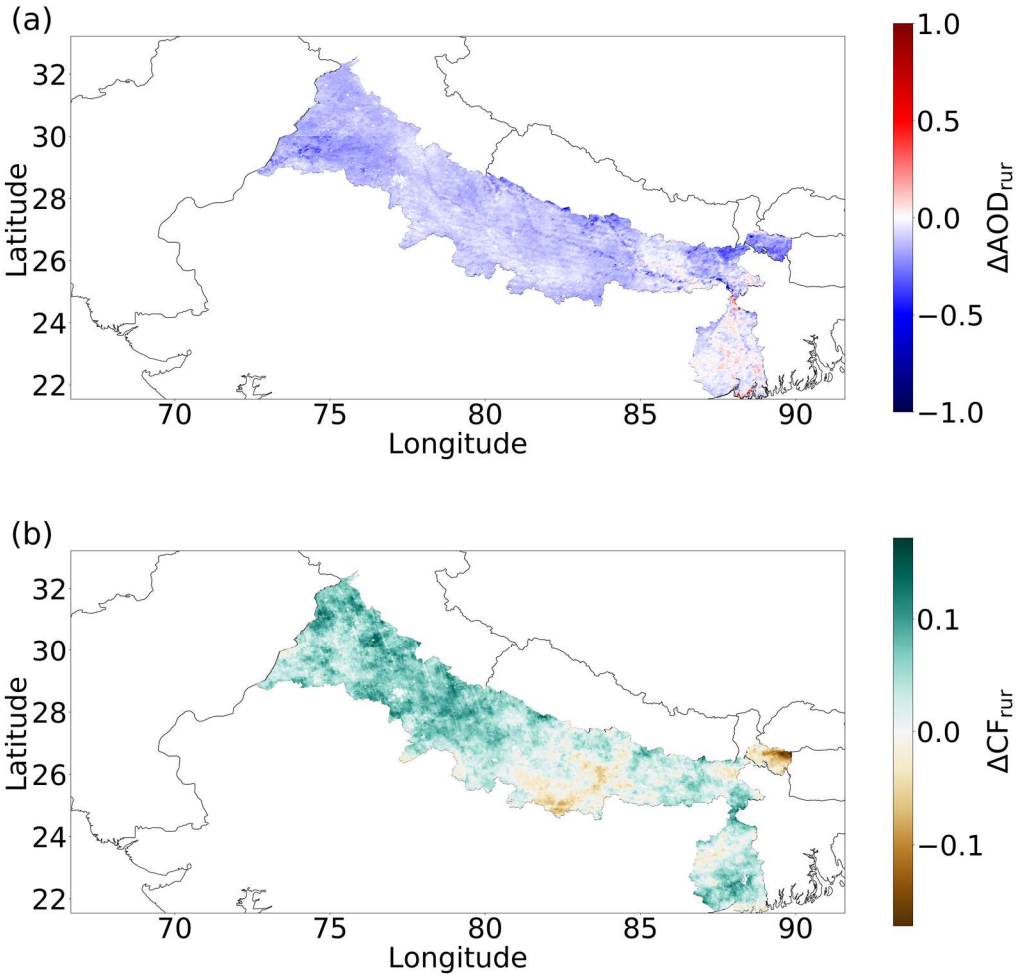

Figure S7: Regional changes in aerosols and clouds. Sub-figures (a) and (b) show maps of the changes in rural aerosol optical depth (AOD_{rur}) and cloud fraction (CF_{rur}) during the lockdown compared to the baseline (5-year for AOD and 1-year for CF).

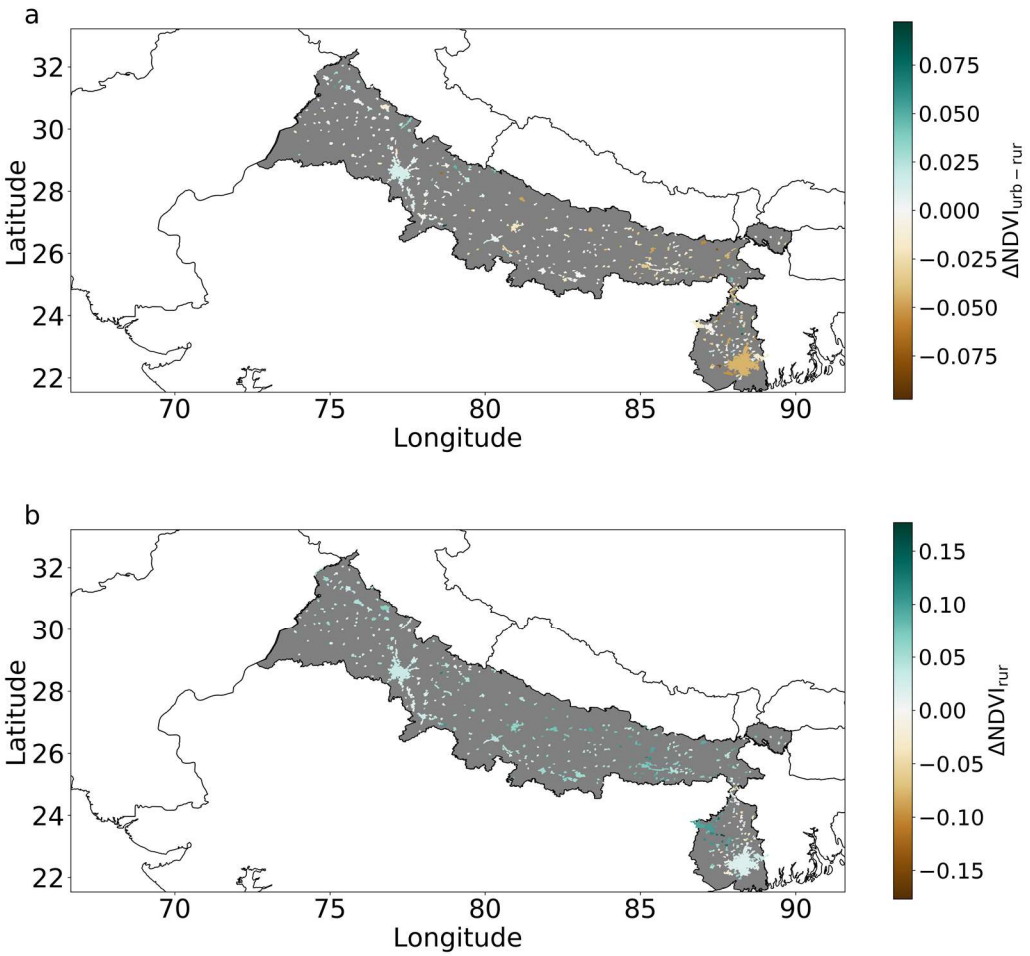

Figure S8: Map of the urban clusters in the region of interest and the change in their (a) spatial mean urban-rural differential in NDVI ($\Delta NDVI_{urb-rur}$) and (b) spatial mean rural NDVI ($\Delta NDVI_{rur}$) during the lockdown compared to the 5-year baseline.

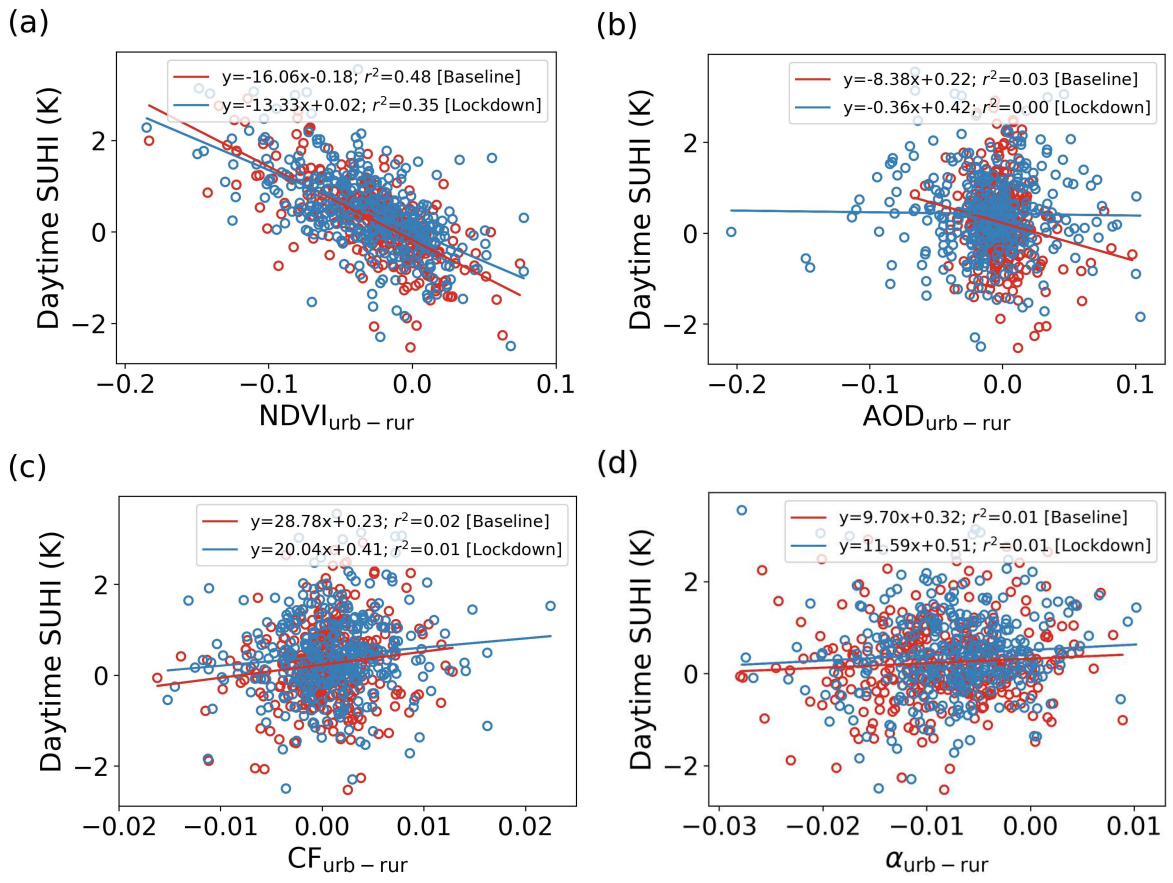

Figure S9: Correlations between surface urban heat islands (SUHI) and the urban-rural differentials in (a) normalized difference vegetation index ($NDVI_{urb-rur}$), (b) Aerosol Optical Depth ($AOD_{urb-rur}$), (c) cloud fraction ($CF_{urb-rur}$), and (d) surface albedo ($\alpha_{urb-rur}$) respectively, for all urban clusters during the lockdown (in blue) and 5-year baseline period (in red). The lines of best fit and coefficients of correlation are shown.

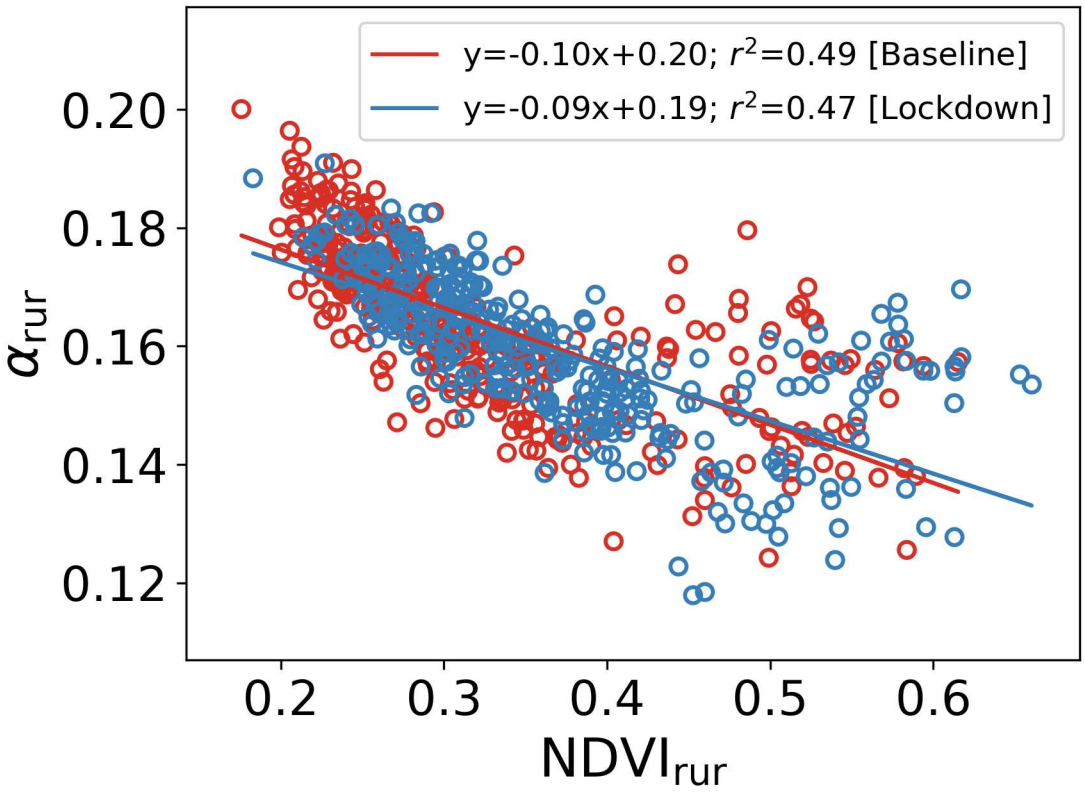

Figure S10: Correlations between surface albedo (α) and normalized difference vegetation index (NDVI), for rural references during the lockdown (in blue) and for the 5-year baseline period (in red). The lines of best fit and coefficients of correlation are shown.

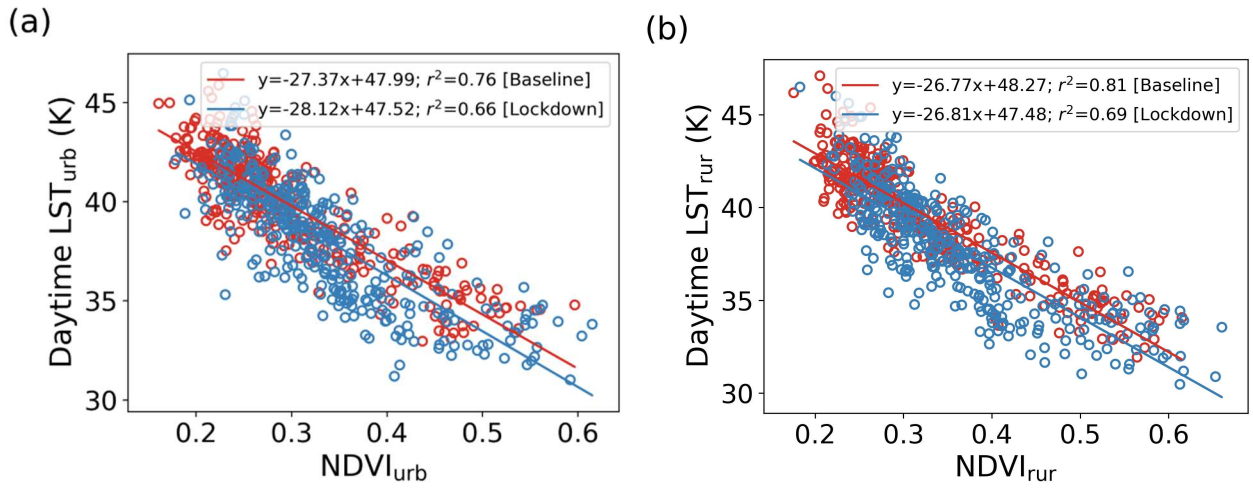

Figure S11: Correlations between land surface temperature (LST) and normalized difference vegetation index (NDVI), for (a) urban clusters and (b) rural references during the lockdown (in blue) and for the 5-year baseline period (in red). The lines of best fit and coefficients of correlation are shown.

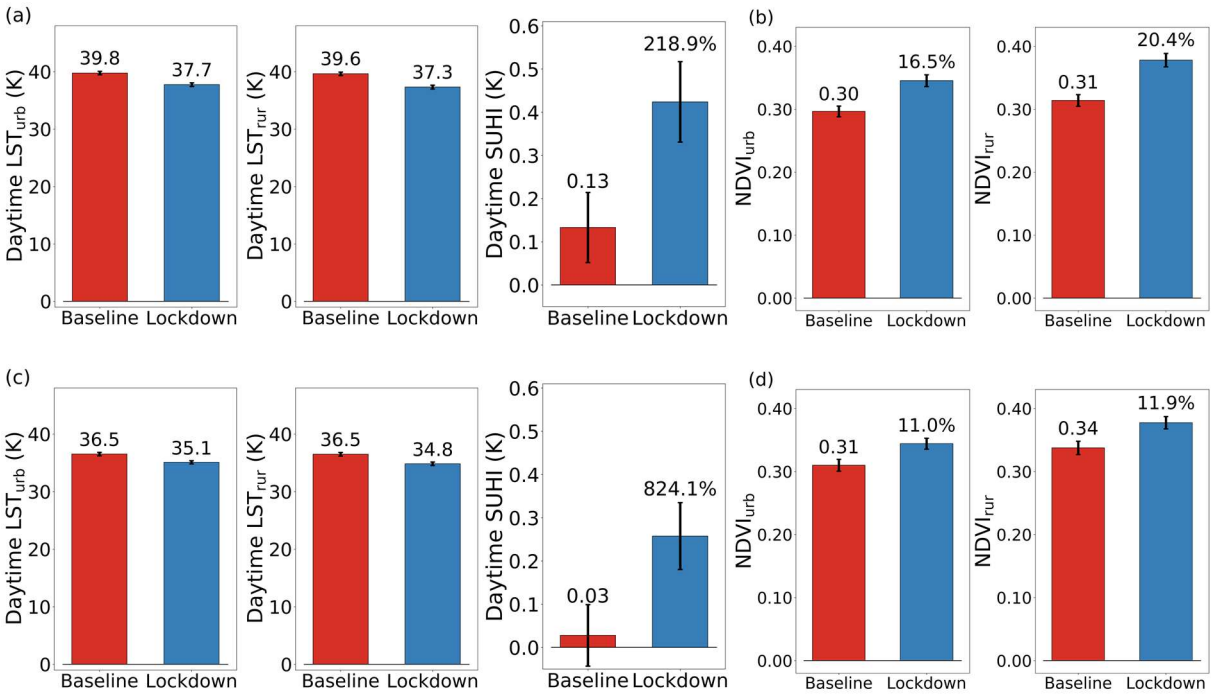

Figure S12: Sensitivity of changes in normalized differences vegetation index (NDVI), land surface temperature (LST), and surface urban heat island (SUHI) to baseline and sensor selection. Sub-figures (a) and (b), show the mean NDVI and LST for urban clusters and their rural references for an 18-year (2003-2019) baseline period, as well as their perturbed values during the lockdown. Sub-figures (c) and (d) are similar, but based on measurements from the Terra satellite and using 5-year (2015-2019) baseline. The error bars represent the 95% confidence interval of the mean.

Table S1: Summary (mean, 95% confidence intervals of mean) of satellite-derived estimates of the main variables of interest for urban clusters and their rural references. The spatial mean of each urban (and corresponding rural) polygon is treated as a sample point.

Variable (unit)	**Satellite Observations**	
	Baseline	Lockdown
Daytime surface urban heat island (K)	(0.23, 0.14, 0.32)	(0.43, 0.34, 0.52)
Nighttime surface urban heat island (K)	(0.88, 0.8, 0.97)	(0.86, 0.78, 0.94)
Urban normalized difference vegetation index	(0.3, 0.29, 0.31)	(0.34, 0.33, 0.34)
Rural normalized difference vegetation index	(0.32, 0.31, 0.33)	(0.37, 0.36, 0.38)
Urban aerosol optical depth	(0.53, 0.53, 0.54)	(0.5, 0.49, 0.51)
Rural aerosol optical depth	(0.54, 0.53, 0.55)	(0.51, 0.5, 0.52)
Urban surface albedo	(0.155, 0.154, 0.157)	(0.151, 0.15, 0.153)
Rural surface albedo	(0.164, 0.162, 0.165)	(0.159, 0.158, 0.16)
Urban cloud fraction	(0.107, 0.102, 0.111)	(0.146, 0.14, 0.151)
Rural cloud fraction	(0.106, 0.102, 0.111)	(0.145, 0.14, 0.15)
Urban daytime surface temperature (K)	(312.9, 312.6, 313.2)	(311.2, 310.8, 311.5)
Rural daytime surface temperature (K)	(312.7, 312.4, 313.0)	(310.7, 310.4, 311.1)
Urban nighttime surface temperature (K)	(295.0, 294.8, 295.1)	(294.4, 294.3, 294.6)
Rural nighttime surface temperature (K)	(294.1, 293.9, 294.3)	(293.6, 293.4, 293.7)

Table S2: Summary of data-driven examination of the control of the urban-rural differentials on the change in SUHI using multiple linear and random forest (RF) regressions. For the linear regressions, the combination of variables that lead to the highest adjusted R^2 is listed for increasing subset size. For the RF regression, both the mean and standard deviation of the permutation feature importance scores and r^2 (based on the 50 random training/validation splits) are noted.

Linear Regressions		**Random Forest Regressions**		
Model	Adjusted R^2	Feature	Importance Scores	r^2
$\Delta SUHI = 0.14 - 9.76 \Delta NDVI_{urb-rur}$	0.15	$\Delta NDVI_{urb-rur}$	0.82 ± 0.08	0.09 ± 0.10
$\Delta SUHI = 0.13 - 9.07 \Delta NDVI_{urb-rur} + 23.54 \Delta \alpha_{urb-rur}$	0.18	$\Delta \alpha_{urb-rur}$	0.46 ± 0.07	
$\Delta SUHI = 0.12 - 8.70 \Delta NDVI_{urb-rur} + 24.08 \Delta \alpha_{urb-rur} - 1.36 \Delta AOD_{urb-rur}$	0.19	$\Delta AOD_{urb-rur}$	0.27 ± 0.04	
$\Delta SUHI = 0.12 - 8.67 \Delta NDVI_{urb-rur} + 24.08 \Delta \alpha_{urb-rur} - 1.39 \Delta AOD_{urb-rur} - 3.61 \Delta CF_{urb-rur}$	0.19	$\Delta CF_{urb-rur}$	0.21 ± 0.03	

Table S3: Regional midday (1:30 pm local time) values (mean ± standard deviation) of relevant variables for the baseline, the lockdown, and their corresponding changes from both the MERRA-2 reanalysis and the satellite observations.

Variable (unit)	MERRA-2 Reanalysis			Satellite Observations		
	Baseline	Lockdown	Change	Baseline	Lockdown	Change
Aerosol optical depth	0.54±0.09	0.44±0.09	-0.1±0.02	0.54±0.11	0.49±0.12	-0.05±0.07
Cloud fraction	0.18±0.05	0.23±0.1	0.05±0.08	0.1±0.05	0.14±0.05	0.04±0.04
Surface temperature (K)	317.4±5	313.5±5.1	-3.9±1.4	313.2±4	311.2±4.2	-2±1.4
Air temperature (K)	311.2±3.6	308.1±3.7	-3.1±1	NA	NA	NA
Relative humidity (%)	18.1±8.2	24.8±7.1	6.7±3.6	NA	NA	NA
Precipitation (mm day^{-1})	0.83±3.2	1.20±3	0.37±0.8	NA	NA	NA
Wind speed (m s^{-1})	4.73±0.7	4.14±0.6	-0.59±0.5	NA	NA	NA
All-sky incident shortwave radiation (W m^{-2})	815.1±56.8	804.6±58.4	-10.5±39.8	NA	NA	NA
Clear-sky incident shortwave radiation (W m^{-2})	867.4±41	880.1±38.9	-12.7±3.7	NA	NA	NA
Clear, clean-sky Incident shortwave radiation (W m^{-2})	949.5±31.4	942.3±28.5	-7.2±3.5	NA	NA	NA
Shortwave aerosol radiative forcing (W m^{-2})	-78.5±12.6	-58.7±13.3	19.8±5.1	NA	NA	NA
All-sky incoming longwave radiation (W m^{-2})	398.9±21.2	396.5±18	-2.4±4.8	NA	NA	NA
Clear, clean-sky incoming longwave radiation (W m^{-2})	390.8±22.5	388.9±21.1	-1.9±4	NA	NA	NA
Clear-sky longwave aerosol radiative forcing (W m^{-2})	4.6±0.8	2.8±0.6	-1.8±0.4	NA	NA	NA
Black-sky albedo	NA	NA	NA	0.164±0.02	0.158±0.182	-0.006±0.008
White-sky albedo	NA	NA	NA	0.181±0.021	0.176±0.019	-0.005±0.009
Surface albedo	0.151±0.02	0.152±0.02	-0.001±0	NA	NA	NA
Normalized difference vegetation index	NA	NA	NA	0.31±0.13	0.35±0.12	0.04±0.04
Sensible heat flux (W m^{-2})	309.5±55	246.4±53.1	-63.1±38.4	NA	NA	NA
Latent heat flux (W m^{-2})	107.7±67.1	198.1±67.2	90.4±39.2	NA	NA	NA
Bowen ratio	2.87±3.02	1.24±0.76	-1.63±2.35	NA	NA	NA